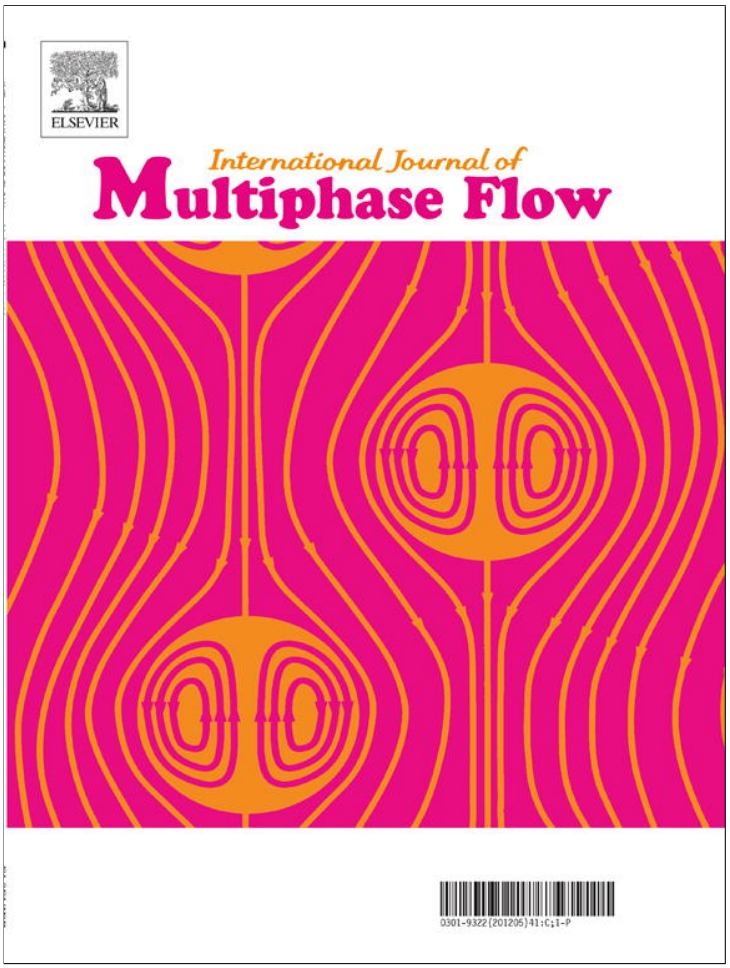

(This is a sample cover image for this issue. The actual cover is not yet available at this time.)

International Journal of Multiphase Flow 48 (2013) 58–70

Contents lists available at SciVerse ScienceDirect

International Journal of Multiphase Flow

journal homepage: www.elsevier.com/locate/ijmulflow

Effects of surfactant on liquid film thickness in the Bretherton problem

Ufuk Olgac, Metin Muradoglu *

Department of Mechanical Engineering, Koc University, Rumelifeneri Yolu, Sariyer, 34450 Istanbul, Turkey

ARTICLE INFO

Article history:
Received 19 May 2012
Received in revised form 21 August 2012
Accepted 22 August 2012
Available online 1 September 2012

Keywords:
Bretherton problem
Dip coating
Liquid film
Bubble dynamics
Surfactant transport
Surfactant solubility
Front-tracking method

ABSTRACT

The effects of insoluble and soluble surfactant on the motion of a long bubble propagating through a capillary tube are investigated computationally using a finite-difference/front-tracking method. Emphasis is placed on the effects of surfactant on the liquid film thickness between the bubble and the tube wall. The numerical method is designed to solve the evolution equations of the interfacial and bulk surfactant concentrations coupled with the incompressible Navier–Stokes equations. A non-linear equation of state is used to relate surface tension coefficient to surfactant concentration at the interface. Computations are first performed for soluble cases and then repeated for the corresponding clean and insoluble cases for a wide range of governing non-dimensional parameters in order to investigate the effects of surfactant and surfactant solubility. The computed film thickness for the clean case is found to be in a good agreement with *Taylor's law* indicating the accuracy of the numerical method. We found that both the insoluble and soluble surfactant generally have a thickening effect on the film thickness, which is especially pronounced at low capillary numbers. This thickening effect strengthens with increasing sensitivity of surface tension to interfacial surfactant coverage mainly due to the enhanced Marangoni stresses along the liquid film. It is also observed that film thickening shows a non-monotonic behavior for variations in Peclet number. The validity of insoluble surfactant assumption is assessed for various non-dimensional numbers and it is demonstrated that insoluble assumption is valid only when capillary number is very low, i.e., $Ca \ll 1$ and when surface tension is highly sensitive to interfacial surfactant coverage, i.e., the elasticity number is large.

1. Introduction

The displacement of liquid by a long gas bubble (or semi-infinite gas finger) moving through a capillary tube is a model widely used to analyze a variety of complex multiphase flow problems. This system was originally studied experimentally by Fairbrother and Stubbs (1935), Taylor (1961) and theoretically by Bretherton (1961). Using a lubrication analysis, Bretherton (1961) related the interfacial pressure drop and liquid film thickness to capillary number, $Ca = \mu U_b/\sigma$, where U_b is the bubble speed, μ is the viscosity of the liquid and σ is the surface tension coefficient in the limit of small Ca and for negligible inertia. His analysis showed that the steady liquid film thickness, h_∞, is related to Ca as $h_\infty/R = 1.34Ca^{2/3}$, where R is the channel radius. This relation was later extended to larger Ca numbers by Ratulowski and Chang (1989). More recently, Aussillous and Quere (2000) fitted a curve to their own and Taylor's original experimental data and put up *Taylor's law* as $h_\infty/R = 1.34Ca^{2/3}/(1 + 2.5 \times 1.34Ca^{2/3})$, where the numerical factor of 2.5 is empirical. Effects of inertia on the Bretherton problem were investigated for relatively higher Reynolds numbers ($Re > 1$, non-creeping flow) by Giavedoni and Saita (1997) and Heil (2001). The liquid–liquid system has been investigated by Hodges et al. (2004) and more recently by Beresnev et al. (2011).

An important issue in multiphase systems is the role played by surface-active agents (surfactants) that are present either as impurities which are difficult to remove from the system or as additives to manipulate the interfacial dynamics. It is well-known that surfactants largely affect the dynamic behavior of deforming interfaces (Levich, 1962; Clift et al., 1978). The presence of surfactants in a fluid mixture can critically alter the motion and deformation of bubbles moving through a continuous liquid phase (Clift et al., 1978; Stone, 1994). Surfactant molecules attach to the interface to form a buffer zone between the gas and liquid phases. They interact with the cohesive forces between the fluid molecules, and thus reduce the surface tension and stabilize the interface (Halpern et al., 2008). The non-uniformity in interfacial surfactant concentration leads to interfacial surface tension gradients and thus Marangoni stresses. Surfactants particularly play a critical role in pulmonary re-opening (Grotberg, 2001, 2011). Pulmonary surfactant is absorbed on the thin film of liquid that covers the surface of the airways and the alveoli and reduces the surface tension on the liquid–gas interface and the work required to expand the lung at each breath. Due to surfactant-deficiency, surface tension on the

* Corresponding author. Tel.: +90 212 338 14 73; fax: +90 212 338 15 48.
E-mail address: mmuradoglu@ku.edu.tr (M. Muradoglu).

0301-9322/$ - see front matter © 2012 Elsevier Ltd. All rights reserved.
http://dx.doi.org/10.1016/j.ijmultiphaseflow.2012.08.007

air–liquid interface might get elevated and the airways might get closed since the flexible structure of the tubes causes instable support for the airways (Heil et al., 2008). Interfacial surfactant dynamics and effects of surfactant on liquid film are thus crucial to understand the pulmonary re-opening process (Grotberg, 2001, 2011).

Influence of surfactants on the displacement of a confined gas–liquid interface has been analyzed analytically (Ginley and Radke, 1989; Ratulowski and Chang, 1990; Park, 1992; Stebe and Barthes-Biesel, 1995; Daripa and Pasa, 2009, 2010), experimentally (Ramdane and Quere, 1997; Shen et al., 2002; Krechetnikov and Homsy, 2005) and numerically (Severino et al., 2003, 2005; Ghadiali and Gaver, 2003; Campana et al., 2010; Johnson and Borhan, 2003; Swaminathan et al., 2010). On the analytical side, Ginley and Radke (1989) assumed a uniform bulk surfactant concentration and studied an adsorption-controlled surfactant transport mechanism and observed higher interfacial concentrations on the thin film compared to the bubble front, and a consequent decrease in the film thickness. Ratulowski and Chang (1990), on the other hand, showed that for trace amount of bulk surfactant, an increase in film thickness occurs when surfactant transport in the bulk is mass-transfer limited and the bulk concentration is not uniform. In this case, if the diffusion of the surfactant from the bubble front to the thin film is slow, lower interfacial concentration on the thin film compared to the bubble front is observed, which leads to development of Marangoni stresses that push more fluid into the thin liquid film region and consequently increase the film thickness. They found, for the first time, that through this mechanism, surfactants could increase the film thickness by a maximum factor of $4^{2/3}$ compared with the surfactant-free case for infinitely long bubbles. In the same surfactant transport regime, Park (1992) confirmed the maximum factor of $4^{2/3}$ through a comprehensive asymptotic analysis for finite length bubbles. Stebe and Barthes-Biesel (1995)'s results support film thickening and the maximum factor of $4^{2/3}$ for elevated bulk surfactant concentrations, and identify the Marangoni stresses that result from hindered sorptive exchange in the thin film as the underlying cause. Daripa and Pasa (2009, 2010) have recently studied the effects of surfactant on the liquid film thickness in the drag-out coating problem and in the long bubbles in capillary tubes problem, respectively, analytically using the lubrication theory and pointed out the thickening effect of surfactant but without giving any explicit expression for the thickening factor.

Experimental studies have mainly focused on the fiber coating (Ramdane and Quere, 1997; Shen et al., 2002) and the plate coating known as the Landau–Levich problem (Krechetnikov and Homsy, 2005). These problems are essentially the same as Bretherton's problem as they all correlate liquid film thickness with capillary number. Ramdane and Quere (1997) performed an experimental study on fibers that are drawn out of a solution containing surfactants and showed that the liquid film that forms on the fiber attains an increased thickness compared to the clean case. They also showed that the thickening factor is dependent on the wire radius and is always smaller than the upper limit predicted theoretically by Ratulowski and Chang (1990). Shen et al. (2002) performed similar experiments using three different surfactants and observed that surfactant generally increases the film thickness until the critical micelle concentration (CMC). Beyond CMC, the behavior is more complicated and depends on the dynamic surface properties. Krechetnikov and Homsy (2005) examined the effects of surfactant on the liquid film thickness for the plate coating. Although their main motivation was to confirm their computational results that film thinning occurs in the presence of surfactant (Krechetnikov and Homsy, 2006), their experimental results showed the opposite (Krechetnikov and Homsy, 2005). They attributed this discrepancy to the fact that pure hydrodynamical modeling of surfactant effects is not sufficient to explain the film thickening. However, Campana et al. (2010) accurately predicted the film thickening for the Landau–Levich problem with numerical solution of the full hydrodynamic problem and found that the numerical results are quantitatively in agreement with the experimental observations of Krechetnikov and Homsy (2005).

Severino et al. (2003, 2005) and Ghadiali and Gaver (2003) computationally investigated the effects of soluble surfactants on the displacement of liquid by a semi-infinite bubble. Severino et al. (2003) considered a planar case while Ghadiali and Gaver (2003) considered axisymmetric cylindrical tube. They both reported results on the effects of various non-dimensional parameters. Severino et al. (2003, 2005) observed film thickening in all situations whereas Ghadiali and Gaver (2003) reported that, depending upon the range of dimensionless parameters, either film thickening or film thinning responses are possible. Johnson and Borhan (2003) and Swaminathan et al. (2010) performed detailed computational analysis of the effects of soluble surfactant on the pressure-driven motion of a gas bubble in a capillary tube using a boundary integral and front-tracking methods, respectively. However they both considered gas bubbles that are comparable to the channel size so no steady liquid film forms between the bubble and the tube wall.

The present study aims to numerically investigate the effects of surfactant and surfactant solubility on the liquid film left on the wall of a cylindrical capillary tube as a gas bubble that is much longer than the tube radius slowly propagates through the tube. For this purpose, the incompressible Navier–Stokes equations are solved fully coupled with the evolution equations of the interfacial and bulk surfactant concentrations using a finite-difference/front-tracking method developed by Muradoglu and Tryggvason (2008). The numerical method has been successfully applied to buoyancy-driven motion of contaminated bubbles rising in a cylindrical tube (Tasoglu et al., 2008). A nonlinear equation of state based on the Langmuir adsorption (Levich, 1962) is used to relate surface tension coefficient to the interfacial surfactant concentration. Although all the computations are performed time-accurately, the focus is placed on the steady-state solutions. A comprehensive computational study is performed to assess the validity of the insoluble surfactant models for this problem. To the best of the authors knowledge, this is the first study that assesses the validity of the insoluble surfactant model through direct numerical simulations. In addition, extensive computations are carried out to investigate the effects of non-dimensional numbers such as elasticity number, Peclet number, Damkohler number and dimensionless adsorption depth on the surfactant dynamics, bubble deformation and film thickness.

The remainder of the paper is organized as follows: In the next section, the mathematical formulation is presented and the numerical method is briefly described. The physical problem is described in Section 3. The results are presented and discussed in Section 4 and some conclusions are drawn in Section 5. Grid convergence of the numerical results is discussed in the Appendix.

2. Formulation and numerical method

In this section the governing equations are described in the context of the finite-difference/front-tracking method. We consider a long gas bubble moving through a liquid filled cylindrical tube of radius R as shown in Fig. 1. The flow is assumed to be incompressible and symmetric about the axis of the tube. The gas bubble and ambient liquid are assumed to be Newtonian fluids. Following Unverdi and Tryggvason (1992), a single set of governing equations can be written for the entire computational domain provided that the jumps in the material properties such as density, viscosity and

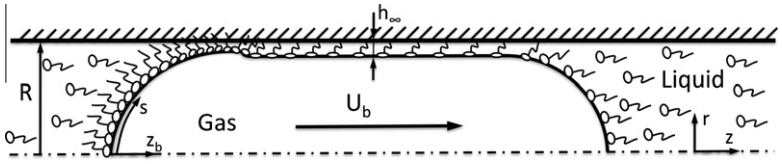

Fig. 1. Schematic illustration of the physical problem and the computational setup.

molecular diffusion coefficient are correctly accounted for and surface tension is included.

In an axisymmetric coordinate system, the Navier–Stokes equations in conservative form are given by

$$\frac{\partial \rho u}{\partial t}+\frac{1}{r}\frac{\partial r\rho u^2}{\partial r}+\frac{\partial \rho u v}{\partial z}=-\frac{\partial p}{\partial r}+\frac{\partial}{\partial r}\left(2\mu\frac{\partial u}{\partial r}\right)+2\mu\frac{\partial}{\partial r}\left(\frac{u}{r}\right)+\frac{\partial}{\partial z}\mu\left(\frac{\partial v}{\partial r}+\frac{\partial u}{\partial z}\right)+\int_A\left(\frac{1}{r}\frac{\partial}{\partial s}(r\sigma t_r)-\frac{\sigma}{r}\right)\delta(\mathbf{x}-\mathbf{x}_f)dA,$$

$$\frac{\partial \rho v}{\partial t}+\frac{1}{r}\frac{\partial r\rho u v}{\partial r}+\frac{\partial \rho v^2}{\partial z}=-\frac{\partial p}{\partial z}+\frac{\partial}{\partial r}\mu r\left(\frac{\partial v}{\partial r}+\frac{\partial u}{\partial z}\right)+\frac{\partial}{\partial z}\left(2\mu\frac{\partial v}{\partial z}\right)+\int_A\frac{1}{r}\frac{\partial}{\partial s}(r\sigma t_z)\delta(\mathbf{x}-\mathbf{x}_f)dA, \quad (1)$$

where u and v are the velocity components in the radial and axial directions, respectively, and p, ρ and μ are the pressure, and the discontinuous density and viscosity fields, respectively. The last term on the right hand side is a body force that includes the effects of surface tension, in which σ is the surface tension coefficient that is a function of the interfacial surfactant concentration Γ, $\mathbf{t} = t_r\mathbf{i}_r + t_z\mathbf{i}_z$ is a unit vector tangent to the interface and s is the arc length along the interface. Note that the mathematical identity $\kappa\mathbf{n}=\frac{\partial \mathbf{t}}{\partial s}$ has been used in Eq. (1), where κ is the curvature of 2D line and $\mathbf{n}$ is the normal vector. The surface tension only acts on the interface as indicated by the three-dimensional delta function δ whose arguments $\mathbf{x}$ and $\mathbf{x}_f$ are the point at which the equation is evaluated and the point at the interface, respectively. The treatment of surface force as a body force was pioneered by Peskin (1977) with the immersed boundary approach. The Navier–Stokes equations are supplemented by the incompressibility condition,

$$\frac{1}{r}\frac{\partial ru}{\partial r}+\frac{\partial v}{\partial z}=0. \quad (2)$$

We also assume that the material properties remain constant following a fluid particle,

$$\frac{D\rho}{Dt}=0;\quad \frac{D\mu}{Dt}=0, \quad (3)$$

where $\frac{D}{Dt}=\frac{\partial}{\partial t}+\mathbf{u}\cdot\nabla$ is the material derivative. The density and viscosity vary discontinuously across the fluid interface and are given by

$$\rho=\rho_b I(r,z,t)+\rho_o(1-I(r,z,t)),\qquad \mu=\mu_b I(r,z,t)+\mu_o(1-I(r,z,t)), \quad (4)$$

where the subscripts "b" and "o" denote properties of the bubble and the ambient fluids, respectively, and $I(r,z,t)$ is the indicator function defined as

$$I(r,z,t)=\begin{cases}1 & \text{in bubble fluid},\\ 0 & \text{in ambient fluid}.\end{cases} \quad (5)$$

Concentration of surfactant on the interface Γ is defined as

$$\Gamma=\frac{dM_s}{dA}, \quad (6)$$

where M_s is the adsorbed mass of surfactant and A is the surface area. Surface tension decreases proportional to the surfactant concentration at the interface according to the equation of state derived from Langmuir adsorption (Levich, 1962),

$$\sigma=\sigma_s+\mathcal{R}T\Gamma_\infty\ln\left(1-\frac{\Gamma}{\Gamma_\infty}\right), \quad (7)$$

where $\mathcal{R}$ is the ideal gas constant, T is the absolute temperature, σ_s is the surface tension of clean interface, and Γ_∞ is the maximum packing concentration. Eq. (7) can also be written as

$$\sigma=\sigma_s\left[1+\beta_s\ln\left(1-\frac{\Gamma}{\Gamma_\infty}\right)\right], \quad (8)$$

where $\beta_s=\mathcal{R}T\Gamma_\infty/\sigma_s$ is the elasticity number. The physicochemical parameter β_s is a measure of the sensitivity of surface tension to variations in interfacial surfactant coverage, Γ/Γ_∞. Following Tasoglu et al. (2008), Eq. (8) is slightly modified to avoid negative values of the surface tension at high interfacial coverage values ($\Gamma/\Gamma_\infty\approx 1.0$):

$$\sigma=\sigma_s\left\{\max\left[\varepsilon_\sigma,1+\beta_s\ln\left(1-\frac{\Gamma}{\Gamma_\infty}\right)\right]\right\}, \quad (9)$$

where ε_σ is taken as 0.05 in the present study. Fig. 2 illustrates the change in surface tension with respect to interfacial surfactant coverage for elasticity numbers employed in this study. Note that the relationship between surface tension and surfactant concentration expressed by Eq. (9) is similar to the experimental data obtained for the pulmonary surfactant survanta by Otis et al. (1994). The surfactant concentration Γ evolves by Stone (1990); Muradoglu and Tryggvason (2008),

$$\frac{1}{A}\frac{D\Gamma A}{Dt}=D_s\nabla_s^2\Gamma+\dot{S}_\Gamma, \quad (10)$$

where the gradient operator along the interface is defined as

$$\nabla_s=\nabla-\mathbf{n}(\mathbf{n}\cdot\nabla). \quad (11)$$

In Eq. (10), A is the area of the interface, D_s is the diffusion coefficient along the interface and $\dot{S}_\Gamma$ is the source term given by

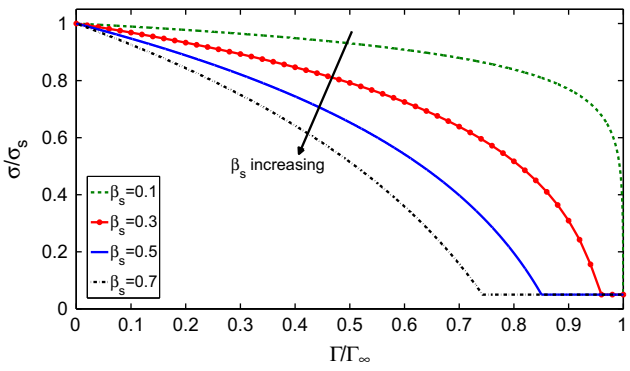

Fig. 2. Sensitivity of surface tension coefficient to interfacial surfactant coverage for a range of elasticity numbers between $\beta_s = 0.1$ and $\beta_s = 0.7$.

$$\dot{S}_\Gamma = k_a C_s(\Gamma_\infty - \Gamma) - k_b\Gamma, \tag{12}$$

where k_a and k_b are the adsorption and the desorption coefficients, respectively, and C_s is the surfactant concentration in the fluid immediately adjacent to the interface. The bulk surfactant concentration C is governed by the advection–diffusion equation

$$\frac{\partial C}{\partial t} + \nabla\cdot(C\mathbf{u}) = \nabla\cdot(D_{co}\nabla C), \tag{13}$$

where the coefficient D_{co} is related to the molecular diffusion coefficient D_c through the indicator function I as

$$D_{co} = D_c[1 - I(r,z,t)]. \tag{14}$$

The source term in Eq. (10) is related to the bulk concentration as

$$\dot{S}_\Gamma = -D_{co}(\mathbf{n}\cdot\nabla C|_{\text{interface}}). \tag{15}$$

Following Muradoglu and Tryggvason (2008), the boundary condition at the interface given by Eq. (15) is first converted into a source term in a conservative manner by assuming that all the mass transfer between the interface and the bulk takes place in a thin adsorption layer adjacent to the interface. In this method, total amount of mass adsorbed on the interface is distributed over the adsorption layer and added to the bulk concentration evolution equation as a negative source term in a conservative manner. Eq. (13) thus becomes

$$\frac{\partial C}{\partial t} + \nabla\cdot(C\mathbf{u}) = \nabla\cdot(D_{co}\nabla C) + \dot{S}_c, \tag{16}$$

where $\dot{S}_c$ is the source term evaluated at the interface and distributed onto the adsorption layer in a conservative manner. With this formulation, all the mass of the bulk surfactant to be adsorbed by the interface is already consumed in the adsorption layer before the interface. Hence, the boundary condition at the interface simplifies to be $\mathbf{n}\cdot\nabla C|_{\text{interface}} = 0$.

The flow equations (Eqs. (1) and (2)) are solved fully coupled with the evolution equations for interfacial concentration, Eq. (10), and for bulk concentration, Eq. (16), by the finite-difference/front-tracking method (Muradoglu and Tryggvason, 2008). A first-order time integration method and a second-order centered difference approximation for the spatial derivatives are used to discretize the momentum, the continuity and the bulk concentration transport equations. A projection method (Unverdi and Tryggvason, 1992; Harlow and Welch, 1965) is used to solve the discretized equations on a stationary, staggered Eulerian grid. Note that it is straightforward to make the numerical method second order accurate in time but the time stepping error is generally found to be negligibly small compared to the spatial error mainly due to small time steps imposed by the stability requirements.

The bubble-ambient fluid interface is tracked using a separate Lagrangian grid which consists of linked marker points (the front) moving with the local flow velocity interpolated from the stationary Eulerian grid. The piece of the Lagrangian grid between two marker points is called a front element. The interfacial surfactant concentration equation, Eq. (10), is solved on the Lagrangian grid using second-order centered differences for the spatial derivatives and a first-order Euler method for the time integration. The Lagrangian grid is also used to calculate the surface tension, which is then distributed onto the Eulerian grid points near the interface by using Peskin's cosine distribution function (Peskin, 1977), and added to the momentum equations as body forces as described by Tryggvason et al. (2001).

Front-tracking method is pioneered by Glimm and colleagues (Chern et al., 1986; Glimm et al., 1998) and the readers are referred to Chern et al. (1986), Glimm et al. (1998), Unverdi and Tryggvason (1992), Tryggvason et al. (2001) for the details of the method. A complete description of the treatment of the soluble surfactant can be found in Muradoglu and Tryggvason (2008) and Tasoglu et al. (2008).

3. Problem statement

The physical problem and computational domain are sketched in Fig. 1. The computational domain is R in radial direction and L_z in the axial direction. The lower boundary is the axis of symmetry representing the centerline of the channel and the flow is in the axial direction. The bubble is initially located at the channel centerline close to the inlet section. The bubble is much longer than the channel width and is initialized with an approximate shape of a straight middle portion and semi-circular front and back menisci. The flow is initiated instantaneously by imposing a fully-developed steady flow at the inlet and keeping the pressure constant at the outlet. Symmetry and no-slip boundary conditions are utilized at the centerline and at the wall of the tube, respectively. The computational domain is set sufficiently long (e.g., up to $L_z/R = 40$) to ensure steady-state motion of bubbles.

The governing equations given in Section 2 are solved in their dimensional forms but the results are expressed in terms of relevant non-dimensional quantities. Utilizing channel radius R and average channel speed U as length and velocity scales, respectively, and $\mathcal{T} = R/U$ the time scale, the governing non-dimensional numbers can be summarized as

$$Re = \frac{\rho_o UR}{\mu_o};\quad Ca_c = \frac{\mu U}{\sigma};\quad Pe_c = \frac{UR}{D_c};\quad Pe_s = \frac{UR}{D_s};\quad \frac{\rho_o}{\rho_b};$$
$$k = \frac{k_a C_\infty}{k_b};\quad Bi = \frac{k_b R}{U};\quad Da = \frac{\Gamma_\infty}{RC_\infty};\quad \beta_s = \frac{\mathcal{R}T\Gamma_\infty}{\sigma_s};\quad \frac{\mu_o}{\mu_b}, \tag{17}$$

where Re, Ca_c, Pe_c, Pe_s, k, Bi, Da, β_s are the Reynolds number, the capillary number based on average channel velocity, the Peclet number based on bulk surfactant diffusivity, the Peclet number based on interfacial surfactant diffusivity, the dimensionless adsorption depth, the Biot number, the Damkohler number and the elasticity number, respectively. Note that C_∞ in Eq. (17) is the bulk concentration at the inlet that is kept constant throughout the computation and is also used as the initial condition in the bulk fluid.

Extensive computations are performed for the soluble, insoluble and clean cases in order to demonstrate the effects of surfactant and surfactant solubility on the liquid film thickness between the wall and the bubble interface. The computations are first performed for the soluble case and then repeated for the corresponding insoluble and clean cases as discussed below. The effects of governing non-dimensional parameters are studied through extensive numerical simulations. For this purpose, we define a base case with nominal parameters and vary only one non-dimensional number at a time while keeping the rest the same as the base case to observe its sole effect on the problem. The non-dimensional numbers for the base case are chosen as $\rho_o/\rho_b = 10$, $\mu_o/\mu_b = 10$, $Re = 1$, $Ca_c = 0.01$, $Pe_c = 100$, $Pe_s = 1000$, $k = 2$, $Bi = 2$, $Da = 0.05$ and $\beta_s = 0.5$. The Reynolds and capillary numbers are usually smaller than those specified here as base case in some applications such as microfluidics (Stone et al., 2004) but these relatively large values are selected mainly to relax the time step restriction and thus facilitate extensive computational simulations. In the present numerical method, the time step is restricted by the CFL condition, i.e., $CFL = \frac{U\Delta t}{\Delta x} \leqslant 1$ where U is the flow speed, Δt is the time step and Δx is the grid size, and by the von Neumann condition, i.e., $\frac{\nu\Delta t}{\Delta x^2} \leqslant \frac{1}{4}$ where ν is the kinematic viscosity. Note that the time step is also restricted by the surface tension but it is less severe compared to CFL and von Neumann conditions, see Muradoglu and Tryggvason (2008) for details. It is emphasized here that the effects of Reynolds number are negligible when $Re < 10$ as discussed by Aus-

sillous and Quere (2000). As shown in the appendix, the relative change in film thickness becomes negligible (below 0.6%) when density and viscosity ratios $\rho_o/\rho_b \geqslant 10$, $\mu_o/\mu_b \geqslant 10$. Therefore computations are performed with $\rho_o/\rho_b = \mu_o/\mu_b = 10$ in order to relax the time step restriction in all the results presented in this paper. The adsorption depth k is set to 2 to have a reasonable interfacial equilibrium concentration, Γ_{eq}. In the equilibrium, adsorption rate is equal to the desorption rate so the surfactant source term is zero. Assuming that there is constant supply of surfactant to the interface ($C_s = C_\infty$) and surfactant source term vanishes, Γ_{eq} can be derived from Eq. (12) as

$$\frac{\Gamma_{eq}}{\Gamma_\infty} = \frac{k}{k+1}, \tag{18}$$

which gives $\Gamma_{eq}/\Gamma_\infty = 2/3$ for $k = 2$. The non-dimensional parameters related to the properties of surfactant are chosen compatible with the physical properties of pulmonary surfactant given by Fujioka and Grotberg (2005) and the references therein (Otis et al., 1994; Schurch et al., 1989) except for the Biot number that is increased up to 2 to achieve a rapid steady-state interfacial surfactant distribution. Elasticity number is taken as 0.5 following Ghadiali and Gaver (2003) and Pe_c and Pe_s are taken as $Pe_c = 100$ and $Pe_s = 1000$ as suggested by Fujioka and Grotberg (2005).

With the above-given non-dimensional parameters, the base case matches the *convective-adsorption model* suggested by Ratulowski and Chang (1990). In this model: (1) Convection is as important as axial diffusion ($Pe \approx O(Ca^{-2/3})$) and hence bulk transport equation must be solved in its full form accounting for both diffusion and convection. (2) Adsorption is in balance with interfacial convection ($St \approx O(Ca^{1/3})$), where $St = k_a\Gamma_\infty/U$ is Stanton number relating the adsorption to the surface convection. Note that $St = k\,Da\,Bi$ in our non-dimensionalization. Therefore the interfacial convection cannot be neglected and interfacial transport equation must be solved coupled with the bulk surfactant concentration and flow equations. Similar conditions were described as *mixed kinetics case* by Ghadiali and Gaver (2003), for which bulk and adsorptive transport rates are comparable and bulk and surface transport equations are coupled and must be solved simultaneously.

For the soluble case, the initial bulk surfactant concentration is specified uniformly as the far field surfactant concentration, C_∞, and the initial interfacial surfactant concentration, Γ_0, is specified to be 40% of the interfacial equilibrium surfactant concentration, Γ_{eq}. The total amount of interfacial surfactant defined as $\Gamma_T = \iint \Gamma\, dA$ is evaluated numerically over the bubble surface at each time step and is monitored to decide if steady-state conditions are reached, i.e., the computations are terminated when the change in Γ_T is less than 0.1% for a period of non-dimensional time $t^* = 1.0$. At the end of each simulation, the effective surface tension coefficient, σ_{eff}, is calculated as

$$\sigma_{\text{eff}} = \sigma_s\left\{\max\left[\varepsilon_\sigma, 1 + \beta_s \ln\left(1 - \frac{\Gamma_{\text{ave}}}{\Gamma_\infty}\right)\right]\right\}, \tag{19}$$

where Γ_{ave} is the steady-state average interfacial surfactant concentration. Then computations are performed for the insoluble and clean cases as follows: For the clean case, both the bulk fluid and the interface are surfactant-free and the surface tension coefficient is taken uniformly as $\sigma = \sigma_{\text{eff}}$. For the insoluble case, the bulk fluid is surfactant-free and adsorption and desorption are switched off. The initial interfacial surfactant concentration is specified uniformly as $\Gamma_0 = \Gamma_T/A_0$ where Γ_T is the total mass of the steady-state interfacial surfactant computed in the soluble case and A_0 is the initial bubble surface area for the insoluble case. Therefore the effective surface tension coefficient σ_{eff} is approximately the same in the soluble, insoluble and clean cases in order to isolate the effects of the Marangoni stress-related mechanisms on the liquid film thickness as much as possible. In all the results presented in this paper, the capillary number is calculated based on this effective surface tension coefficient, i.e., $Ca = \mu U_b/\sigma_{\text{eff}}$.

4. Results and discussion

Extensive computational simulations are carried out to examine the effects of surfactant and surfactant solubility on the liquid film thickness in Bretherton problem. A uniform regular Cartesian grid is employed in all the results presented here. A comprehensive grid convergence study is performed to determine the minimum grid size required to reduce the spatial discretization error below a threshold value. As detailed in the Appendix, we found that a grid containing about 64 grid cells in the radial direction is sufficient to reduce the spatial discretization error in the film thickness below 5%. Thus computations are performed using a uniform grid containing at least 64 grid cells in the radial direction in all the results presented in this paper except for the low capillary number cases, i.e., $Ca < 0.004$, for which a twice finer grid containing 128 grid cells in the radial direction is utilized in order to resolve the thin liquid film region.

Extensive computational simulations are performed to examine the effects of the governing non-dimensional parameters. First computations are performed for a range of capillary numbers while keeping the other parameters the same as the base case. Fig. 3 shows the steady distribution of the interfacial and bulk surfactant concentrations for various capillary numbers. It is seen that interfacial surfactant distribution becomes less uniform as the capillary number increases mainly due to enhanced convection. The liquid film gets thicker as Ca increases and thus more liquid is pumped into the film region. The surfactant is absorbed onto the interface and convected towards the stagnation point on the trailing edge of the bubble where it is accumulated and eventually desorbed back into the bulk fluid when the concentration exceeds the equilibrium value as can be seen in Fig. 3c and d. On the other hand, at low Ca, the film is very thin and bulk surfactant transport from the leading to the trailing edge is poor. This results in a relatively more uniform interfacial surfactant distribution. This is better seen in Fig. 4 where the interfacial surfactant concentration, the surface tension coefficient, the Marangoni stress and the film thickness are plotted for various capillary numbers. Note that the Marangoni stress, $\tau_M = \frac{d\sigma}{ds}$, is non-dimensionalized and is expressed in terms of the Marangoni number defined as $Ma = \frac{\tau_M}{\tau_{\text{vis}}}$ where $\tau_{\text{vis}} = \mu_o \frac{U}{R}$ represents the viscous stresses. It is interesting to observe that, in the limit of very low capillary number, i.e., $Ca = 0.0015$, the interfacial surfactant distribution is nearly uniform and the bubble assumes

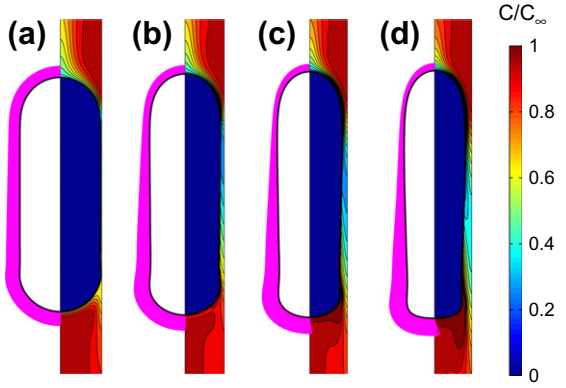

Fig. 3. Soluble model: steady-state interfacial surfactant concentration (left side) and bulk surfactant concentration (right side) for various Ca numbers. (a) $Ca = 0.0015$, (b) $Ca = 0.016$ (base case), (c) $Ca = 0.044$ and (d) $Ca = 0.097$.

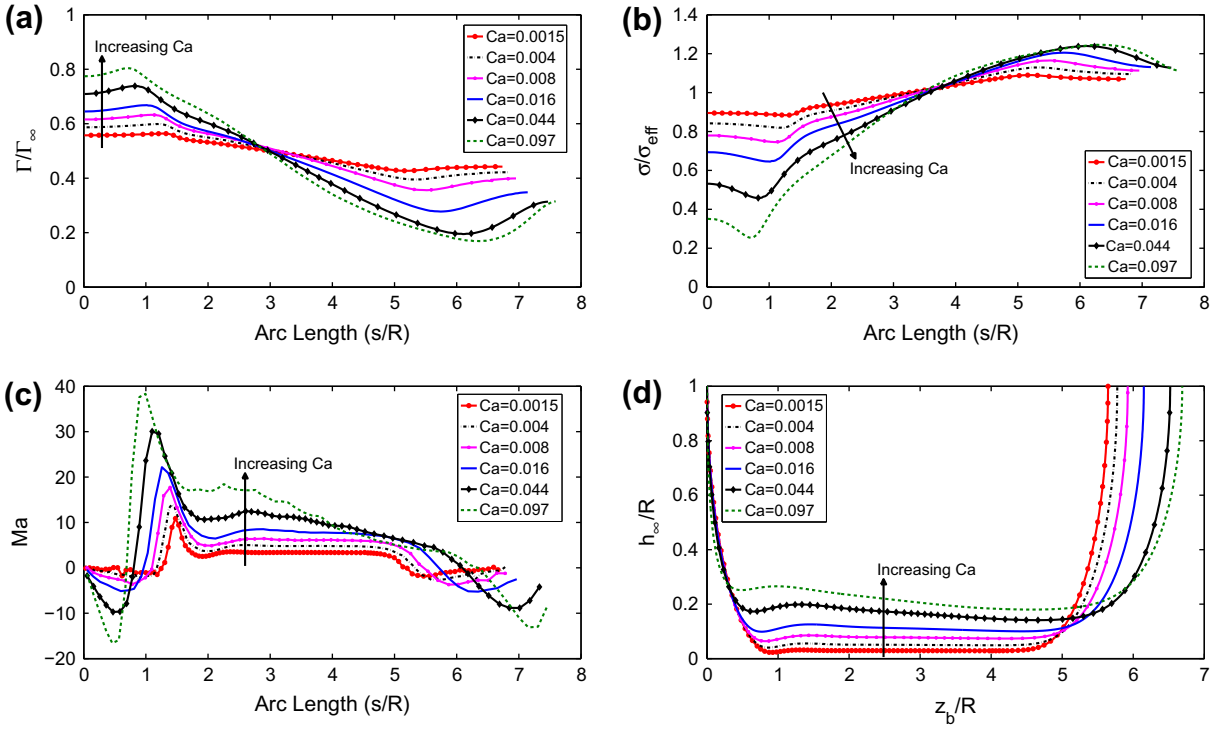

Fig. 4. Soluble model: the steady-state distributions of (a) interfacial surfactant concentration, (b) surface tension coefficient, (c) Marangoni stress and (d) film thickness for a range of capillary numbers.

essentially the same shape of a clean interface mainly due to small Marangoni stresses (see Fig. 6a for comparison with the clean case). As *Ca* increases, the film thickens and thus surfactant is more easily convected to the trailing edge as shown in Fig. 4a. This results in sharper gradients in interfacial surfactant distribution and thus leads to elevated Marangoni stresses (Fig. 4a and c). For moderate *Ca* values ($Ca = 0.004 - 0.016$), the Marangoni stress over the liquid film is more uniform and has approximately the same magnitude as the opposing Marangoni stress on the leading front, which results in a more uniform film thickness. For high capillary numbers ($Ca = 0.044$ and 0.097), the Marangoni stress over the liquid film is no more uniform and is less than the opposing stress on the leading front, which pushes more liquid into the film region resulting in further non-uniform thickening. Fig. 5 shows the variation of the film thickness as a function of capillary number for the soluble, insoluble and clean cases. The film thickness is evaluated at the mid-point of the bubble (defined as the middle point of the two tip points of the bubble on axis) for all the cases so it represents somewhat average film thickness for large capillary numbers for which the film thickness is no more uniform for the contaminated cases as seen in Fig. 4d. Note that, although it is also plotted in Fig. 5, the film thickness computed using the insoluble model becomes unphysical when the capillary number is large as will be discussed later. *Taylor's law* (Aussillous and Quere, 2000) and the maximum thickening predicted by Ratulowski and Chang (1990) are also shown in Fig. 5. As can be seen, the numerical results for the clean cases are in a good agreement with *Taylor's law*, which indicates the accuracy of the computational results. Note that the maximum difference between the computed clean film thickness and *Taylor's law* is less than 8% for the range of capillary numbers studied here. In the soluble case, the film thickness increases considerably for low *Ca* and assumes approximately the same values as the clean cases for high *Ca* mainly because viscous forces become dominant over the surface tension forces as *Ca* increases. This is in qualitative agreement with the experimental results of Krechetnikov and Homsy (2005) who reported a similar trend that the presence of surfactants generally leads to film thickening which is pronounced at low *Ca* (thin films) and gets weaker as *Ca* increases (thick films). Similarly, Severino et al. (2003) also found computationally that the effects of surfactant on the film thickness are no longer noticeable when *Ca* is larger than a certain value. Fig. 5 also shows that the computed film thickness is always below the upper limit that is predicted by Ratulowski and Chang (1990) and is obtained by multiplying *Taylor's law* with the maximum increase factor of $4^{2/3}$. The insoluble model predicts slightly smaller film thickness compared to the soluble model for the small capillary numbers, i.e., $Ca < 0.025$. Comparison for larger values of the capillary number is not meaningful since the insoluble model gives unphysical solutions especially at the back of the bubbles as mentioned before.

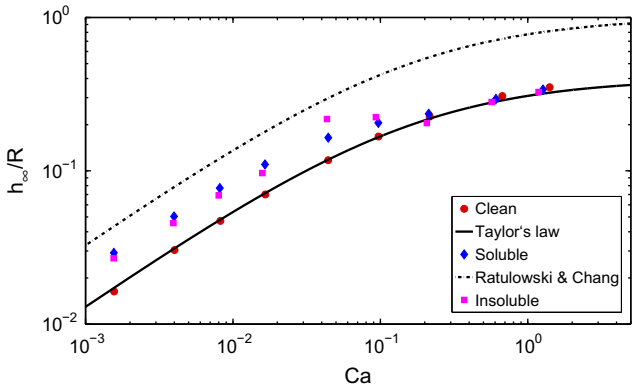

Fig. 5. Film thickness computed using the clean, insoluble and soluble models for various capillary numbers. Solid line represents *Taylor's law* ($h_\infty/R = 1.34Ca^{2/3}/(1 + 1.34 \times 2.5Ca^{2/3})$) Aussillous and Quere (2000) and solid-dotted line represents the upper limit of the film thickness achievable with the introduction of surfactants as suggested by Ratulowski and Chang (1990).

We then examine the effects of surfactant solubility in more detail for the same range of capillary numbers. For this purpose, the interfacial surfactant concentration, surface tension coefficient, Marangoni stress and film thickness are plotted in Fig. 6 for soluble, insoluble and clean cases. It is observed that, for low *Ca*, i.e., *Ca* = 0.0015, the discrepancy between the soluble and insoluble cases is negligibly small whereas the discrepancy gets more pronounced as *Ca* increases. This is mainly due to the lack of surfactant supply at the leading meniscus and excessive surfactant accumulation at the trailing edge of the bubble in the insoluble case. As *Ca* increases, the liquid film becomes thicker and the interfacial surfactant at the leading meniscus is easily convected to the trailing edge of the bubble. In the base case of *Ca* = 0.016 (Fig. 6b), the film thickness is predicted slightly thinner in the insoluble case than that in the soluble case. At higher *Ca*, e.g., *Ca* = 0.044 (Fig. 6c), in the insoluble case, there occurs a surfactant-free region after the stagnation point on the leading edge of the bubble resulting in elevated Marangoni stresses and thus a thicker film prediction compared to the soluble case. At even higher *Ca*, e.g., *Ca* = 0.097 (Fig. 6d), in the insoluble case, this trend is more pronounced

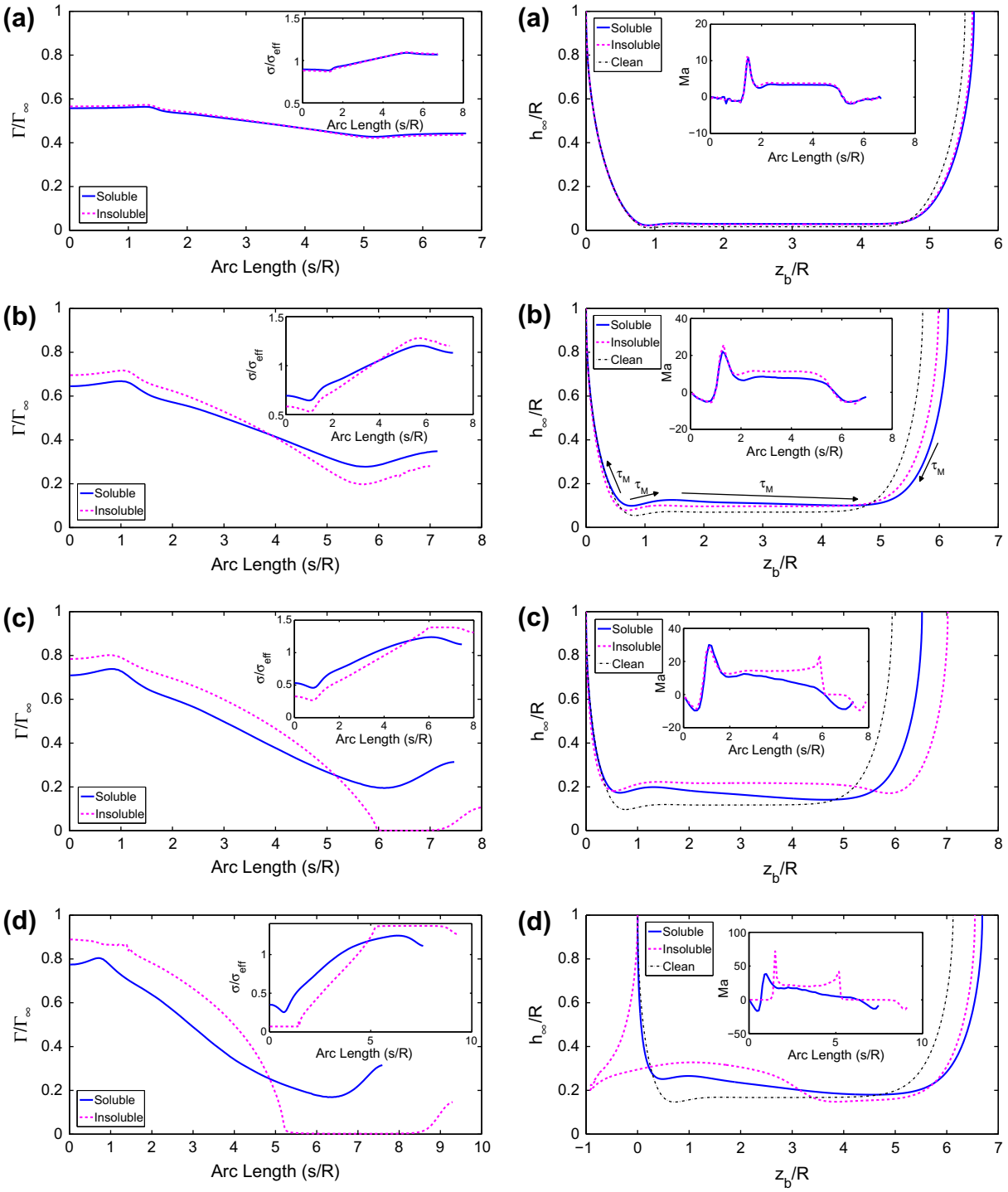

Fig. 6. The interfacial surfactant distribution and surface tension (inset) for soluble and insoluble cases (left side), and the film thickness and Marangoni stress (inset) for soluble, insoluble and clean cases (right side) for various *Ca* numbers. (a) *Ca* = 0.0015, (b) *Ca* = 0.016 (base case), (c) *Ca* = 0.044 and (d) *Ca* = 0.097.

and the leading half of the bubble behaves like a clean interface and thus yields a thinner film prediction whereas the liquid film becomes thicker than that of soluble case in the trailing half of the bubble due to the elevated Marangoni stresses resulting from sharp surfactant concentration gradient, resembling the stagnant-cap observed in buoyancy-driven gas bubbles (Tasoglu et al., 2008). In summary, the insoluble surfactant model predicts slightly thinner films compared to the soluble model at low capillary num-

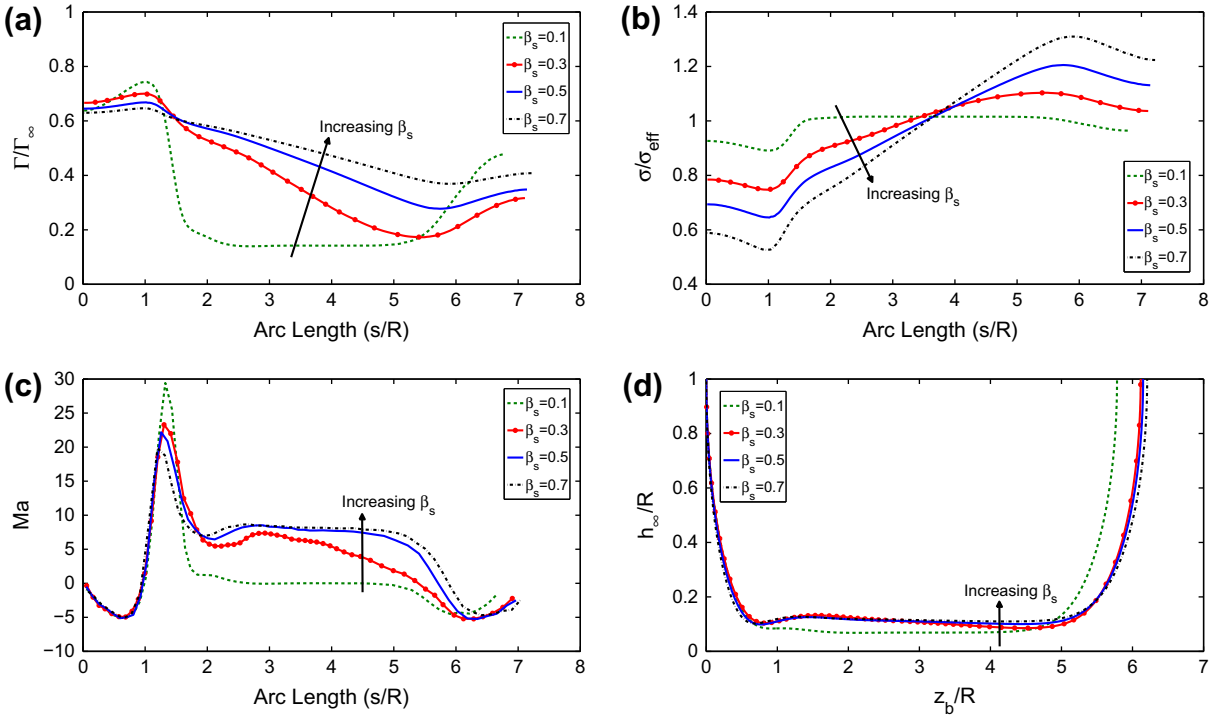

Fig. 7. The effects of the elasticity number for the soluble case. (a) Interfacial surfactant concentration, (b) surface tension coefficient, (c) the Marangoni stress and (d) film thickness computed for a range of β_s.

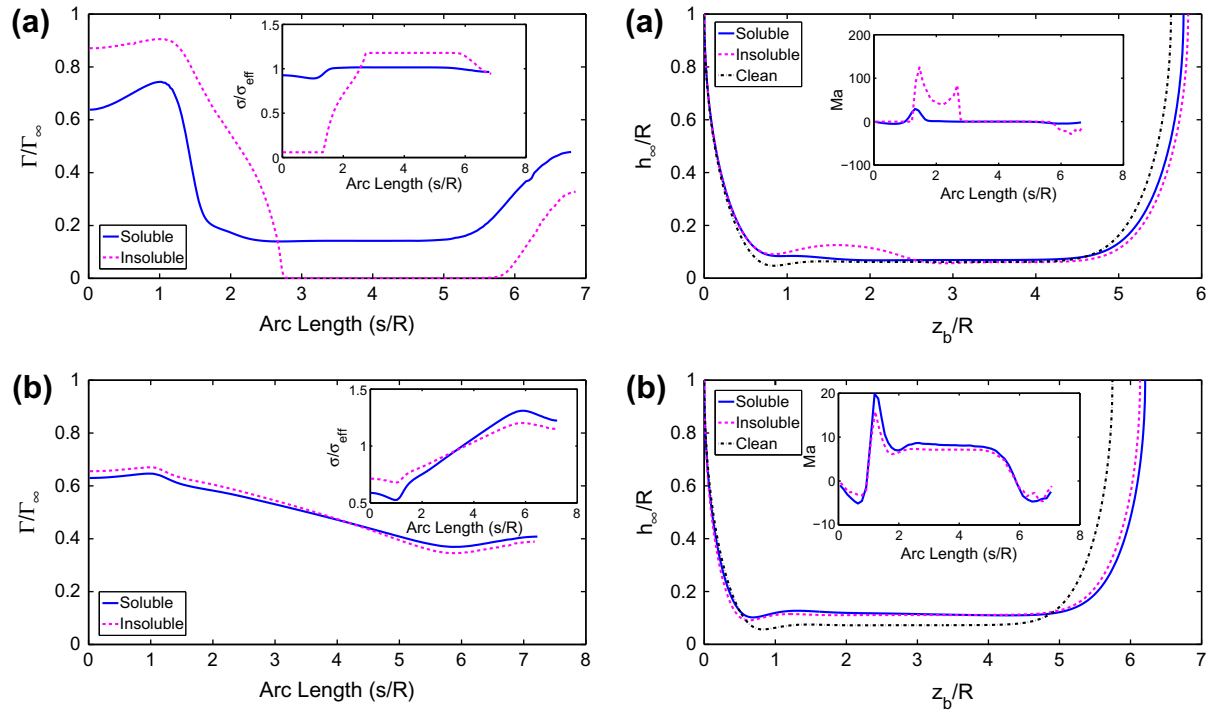

Fig. 8. The interfacial surfactant distribution and surface tension (inset) for soluble and insoluble cases (left side), and the film thickness and Marangoni stress (inset) for soluble, insoluble and clean cases (right side) for the elasticity number of (a) $\beta_s = 0.1$ and (b) $\beta_s = 0.7$.

bers. As *Ca* increases, the insoluble model first assumes a thicker film and then leads to ambiguous predictions in film thickness with further increase in *Ca*.

Computations are then performed to examine the effects of elasticity number. For this purpose, the elasticity number β_s is varied between 0.1 and 0.7 while other parameters are kept the same as the base case. The surface tension decreases more abruptly with increasing interfacial surfactant coverage as β_s increases (see Fig. 2). Increasing β_s results in larger Marangoni stresses which oppose to the viscous shear stresses and act to reduce the mobility of the interface. Therefore the interfacial surfactant concentration is expected to become more uniform due to reduced mobility of the interface as β_s increases (see Fig. 7). Conversely, as β_s decreases, surface tension gets less sensitive to interfacial surfactant concentration leading to lower Marangoni stresses and higher mobility of the interface. As a result, the surfactant adsorbed on the leading meniscus are easily advected along the interface and accumulated at the trailing meniscus of the bubble (see Fig. 7). At the very low elasticity numbers, i.e., $\beta_s = 0.1$, the bubble behaves like a clean bubble except for the trailing edge (see Fig. 8a for comparison with the clean case). Although the surface tension is less sensitive to interfacial surfactant coverage for $\beta_s = 0.1$, the sharp gradient in surfactant concentration due to the accumulated mass of surfactant at the trailing edge is sufficient to produce the highest Marangoni stress at this location among all cases. This Marangoni stresses push liquid into the film and deform the interface at the trailing edge as demonstrated in Fig. 7d. For $\beta_s = 0.3$, the Marangoni stress over the liquid film is non-uniform resulting in a non-uniform film thickness as shown in Fig. 7c and d. As β_s increases, the liquid film becomes more uniform as a result of enhanced Marangoni stresses. The interfacial surfactant concentration and liquid film thickness are plotted for the clean, insoluble and soluble cases in Fig. 8 for $\beta_s = 0.1$ and $\beta_s = 0.7$. It is seen that film thickening is negligible for $\beta_s = 0.1$ for most part of the interface except for the trailing edge of the bubble whereas significant thickening is observed for $\beta_s = 0.7$. Fig. 8 also shows that the effect of surfactant solubility is small at high elasticity numbers while the solubility becomes more important as the elasticity number decreases. It is seen that there is significant discrepancy between the soluble and insoluble cases at low elasticity number, i.e., $\beta_s = 0.1$, as can be clearly seen especially in the interfacial surfactant concentration. When the elasticity number is small, the surfactant is convected easily towards the trailing edge and accumulated near the stagnation point both for the soluble and insoluble cases. The surfactant is desorbed back into the ambient fluid when the concentration exceeds the equilibrium value in the soluble case. However, in the case of insoluble model, the surfactant continues to accumulate near the stagnation point until the surfactant gradient becomes sufficiently large so that the resulting Marangoni stresses can balance the viscous shear stresses. This results in stag-

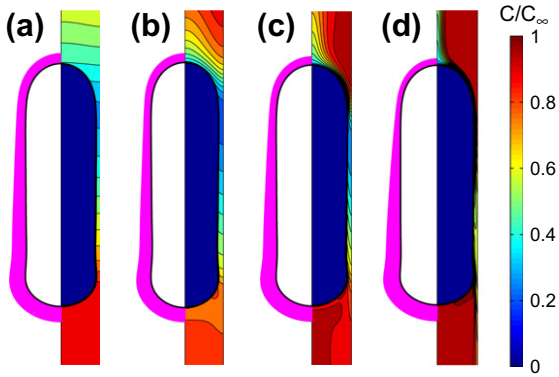

Fig. 9. The effects of the Peclet number in the soluble case. The steady-state interfacial surfactant concentration (left side) and bulk surfactant concentration (right side) for the Peclet numbers of (a) $Pe_c = 1$, $Pe_s = 10$, (b) $Pe_c = 10$, $Pe_s = 100$, (c) $Pe_c = 100$, $Pe_s = 1000$ (base case) and (d) $Pe_c = 1000$, $Pe_s = 10000$.

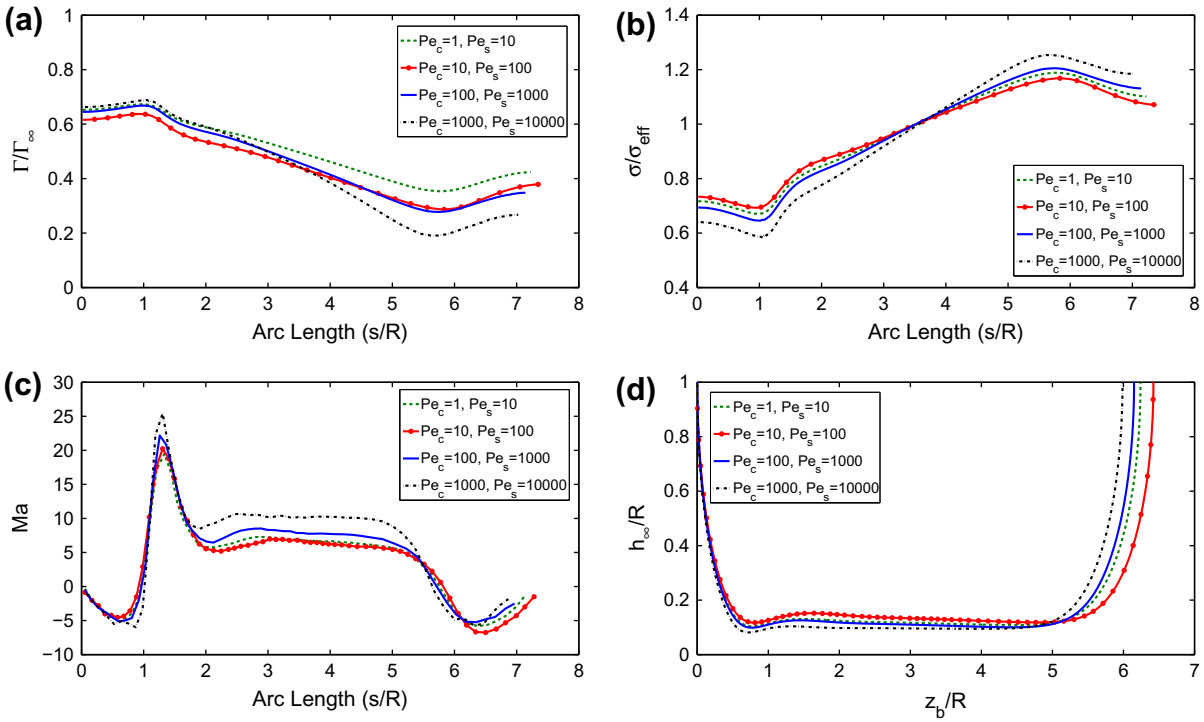

Fig. 10. The effects of the Peclet number in the soluble case. The steady-state distributions of (a) the interfacial surfactant concentration, (b) surface tension coefficient, (c) Marangoni stress and (d) film thickness.

nant-cap like surfactant distribution at the interface in the insoluble case when the elasticity number is small. However, unlike the stagnant-cap, some surfactant remains at the leading edge due to the existence of the stagnation point there. We thus conclude that the solubility becomes more important and insoluble models result in inaccurate predictions at low β_s.

Next the effects of Peclet number are studied by varying Pe_c and Pe_s in the range $(1–10^3)$ and $(10–10^4)$, respectively, while keeping the other parameters the same as the base case. Bulk and surface Peclet numbers are varied together proportionally. Fig. 9 demonstrates the interfacial and bulk surfactant distribution for various *Pe* numbers. When *Pe* is small, i.e., $Pe_c = 1$, diffusion dominates over convection and the iso-concentration lines are almost perpendicular to the tube wall suggesting that the convection plays a very minor role in bulk surfactant distribution. On the other hand, when *Pe* increases, e.g., $Pe_c = 1000$, convection dominates and we observe a thin boundary layer over the interface with sharp gradient of bulk surfactant concentration. Fig. 10 shows the interfacial surfactant concentration, surface tension coefficient, Marangoni stress and film thickness for various *Pe* numbers. It can be seen in this figure that Peclet number has significant influence on the steady motion of the bubble but, although not shown here, its effects are more pronounced in the transient period. At low *Pe*, i.e., $Pe_c = 1$, the diffusion dominates over the convention as also mentioned above so a large amount of bulk surfactant is carried onto the interface by diffusion resulting in elevated surfactant concentration at the interface. When Pe_c is increased to 10, the interfacial surfactant concentration drops homogeneously as convection hinders diffusive transport to the near-interface region. Further increase in *Pe* results in a lower bubble-tip concentration and a sharper surfactant distribution along the liquid film. Although the influence of the Peclet number is not very large in the range of Peclet numbers studied here, it is interesting to see that Marangoni stress at the leading edge first increases and then decreases as Peclet number increases. This non-monotonic behavior is also reflected on the liquid film thickness response as demonstrated in Fig. 10d. Further computations are performed to more accurately quantify the effects of the Peclet number on the film thickness and the results are plotted in Fig. 11. This figure clearly shows the non-monotonic behavior and the film thickness assumes its peak value about $Pe_c = 10$. Note that this peak value is still smaller than the upper limit predicted theoretically by Ratulowski and Chang (1990). It is emphasized here that the non-monotonic behavior in film thickness is qualitatively in agreement with the results obtained for the case of semi-infinite gas finger by Ghadiali and Gaver (2003) and for the plate coating by Severino et al. (2005) where the peak film thickness is predicted at about $Pe_c = 10$ and 30, respectively.

The bulk surfactant concentration can be easily changed in experimental studies. Therefore we finally perform extensive computational simulations to examine the effects of the bulk surfactant concentration on the liquid film thickness instead of the related non-dimensional parameters of Damkohler number and adsorp-

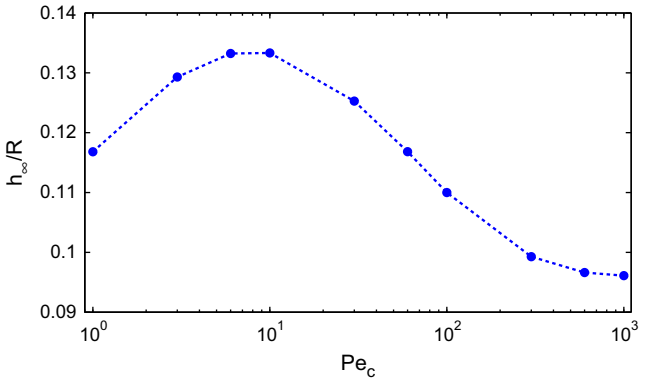

Fig. 11. Variation of the film thickness as a function of the Peclet number for the soluble case.

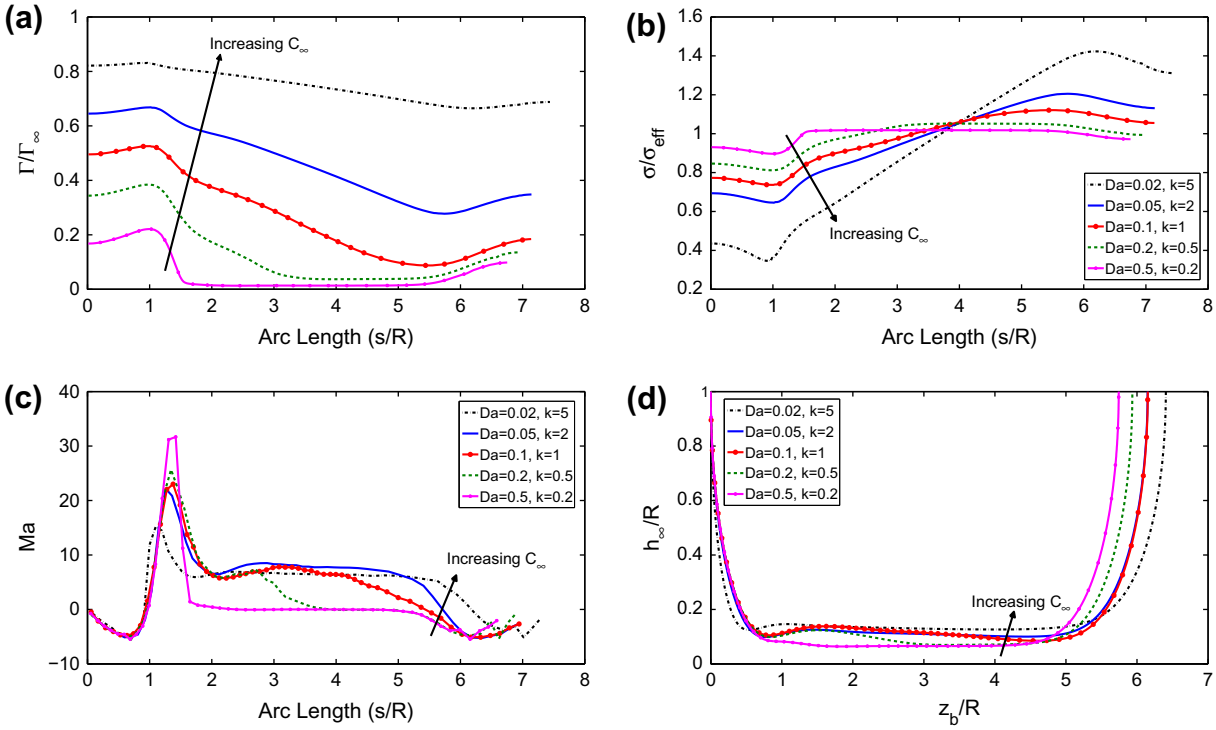

Fig. 12. The effects of the bulk surfactant concentration in the soluble case. The steady-state distributions of (a) the interfacial surfactant concentration, (b) surface tension coefficient, (c) Marangoni stress and (d) film thickness computed for a range of the Damkohler number and the adsorption depth.

tion depth. For this purpose, Da and k are varied in such a way that the net effect is to change the bulk surfactant concentration while keeping the other parameters the same as the base case. Computations are performed for Da and k in the range 0.02–0.5 and 5–0.2, respectively. Note that Γ_{eq} correspondingly deviates from its base case value as C_∞ changes according to Eq. (18). Fig. 12 illustrates the interfacial surfactant concentration, surface tension coefficient, Marangoni stress and film thickness for various values of C_∞. The liquid film thickness is also plotted in Fig. 13 for three values of C_∞ for clean and contaminated (soluble) cases. For small values of C_∞, e.g., $Da = 0.5$ and $k = 0.2$, only scarce amount of surfactant is accumulated at the trailing edge of the bubble and the bubble assumes nearly the same shape of a clean bubble (see Fig. 13a). In this case, the sharp gradient of surfactant concentration at the trailing edge results in enhanced local Marangoni stresses that cause significant deformation in the trailing edge of the bubble as seen in Fig. 12c and d. When C_∞ increases, the interfacial concentration increases non-uniformly resulting in a non-uniform film thickness. With further increase in C_∞, Marangoni stress becomes more uniform over the liquid film resulting in a more uniform film thickness. The thickening effect is most obvious for the intermediate values of C_∞, i.e., $Da = 0.1$ and $k = 1$, as seen in Fig. 13b. In this case, the amount of bulk surfactant is sufficient to cause significant Marangoni stress at the interface but small enough to avoid the complete saturation of the interface. In the limit of very high bulk surfactant concentration, i.e., $Da = 0.02$ and $k = 5$, the interface is covered with the surfactant almost uniformly. As a result, the surface tension reduces nearly uniformly over the interface leading to very small Marangoni stresses. In this case, the bubble behaves like a clean bubble with small surface tension coefficient and the Marangoni-induced thickening effect is less pronounced as can be seen in Fig. 13c.

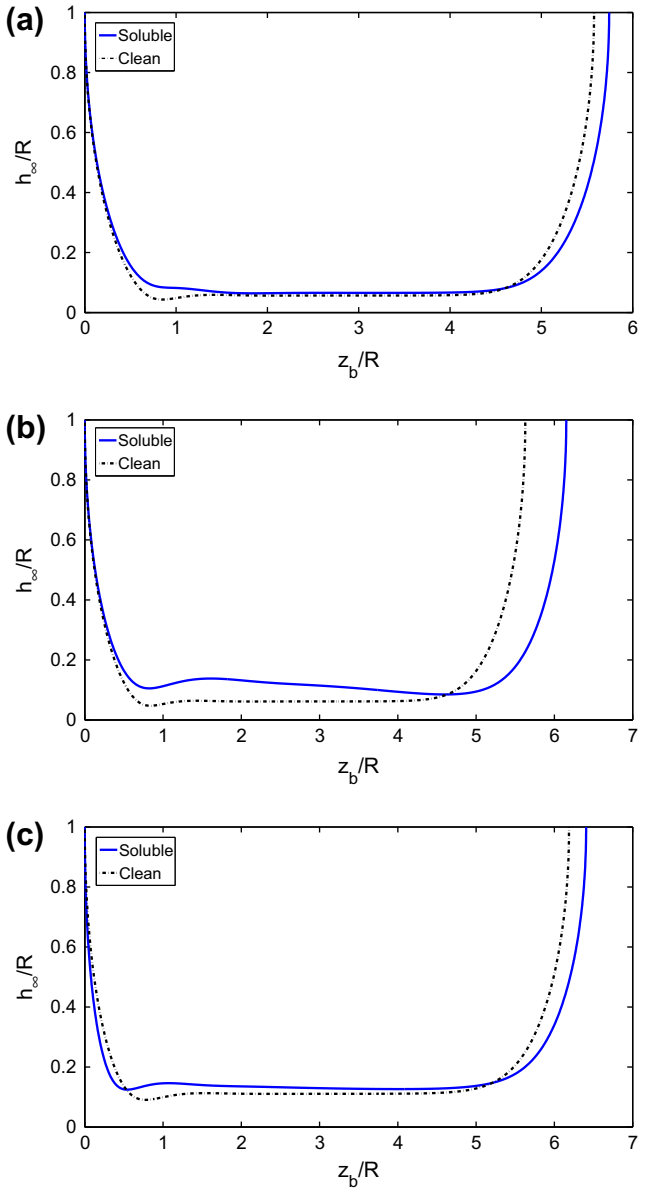

Fig. 13. Comparison of liquid film thickness for (a) $Da = 0.5$, $k = 0.2$, (b) $Da = 0.1$, $k = 1.0$ and (c) $Da = 0.02$, $k = 5.0$. The bulk surfactant concentration C_∞ increases from left to right.

5. Conclusions

The effects of soluble and insoluble surfactants on the motion and deformation of a gas bubble in a horizontal axisymmetric channel are computationally studied by using a finite-difference/front-tracking method. The Navier–Stokes equations are solved fully coupled with the bulk and interfacial surfactant concentration evolution equations, and the surface tension is related to the interfacial surfactant concentration using a nonlinear equation of state based on the Langmuir kinetics.

The liquid film thickness is first compared with *Taylor's law* (Aussillous and Quere, 2000) for the clean cases and it is found that the computational results are in a good agreement with *Taylor's law* for a wide range of capillary numbers. Then extensive computations are performed to study the effects of insoluble and soluble surfactants on the steady-state liquid film thickness between the bubble and the tube wall. It is found that the presence of surfactants generally increases the liquid film thickness due to the Marangoni stresses that develop on the interface. Thickening effect of surfactants is more pronounced at low capillary numbers and diminishes as capillary number increases. The surfactant-induced thickening of the liquid film is found to be within the theoretical limits predicted by Ratulowski and Chang (1990). Elasticity number, β_s, significantly changes the surfactant concentration distribution on the interface. As β_s increases, the surface mobility decreases due to increasing Marangoni stresses along the liquid film leading to more uniform interfacial surfactant distribution. It is found that the film thickening effect is pronounced as β_s increases. The effects of the Peclet number are also examined. It is found that the Peclet number has a non-monotonic influence on the film thickness and the maximum film thickness is obtained at about $Pe_c = 10$. Changing far field bulk surfactant concentration, C_∞, also affects the bubble dynamics significantly and the maximum thickening effect occurs at intermediate values of C_∞. Excessive increase in C_∞ results in complete saturation of the interface with the surfactant, which leads to nearly uniform interfacial surfactant concentration and thus diminishing the Marangoni stresses.

Further computations are performed to evaluate the validity of the insoluble surfactant models. It is found that the insoluble models are only valid for very-low capillary and high elasticity numbers. It is also found that the insoluble models may lead to qualitatively inaccurate results especially when the mobility of the bubble interface is high, i.e., in the high capillary number and low elasticity number limits.

Acknowledgments

The authors are grateful to the Scientific and Technical Research Council of Turkey (TUBITAK) for support of this research through Grant 108M238 and Turkish Academy of Sciences through TUBA-

GEBIP program. The first author (UO) is supported by TUBITAK through BIDEB.

Appendix A. Grid convergence and effects of density and viscosity ratios

A.1. Grid convergence

Extensive computations are first performed in this section to show the grid convergence and determine the minimum grid size required to reduce the spatial discretization error below 5%. For this purpose, computations are performed for the base case using four sets of uniform regular Cartesian grids containing 16, 32, 64 and 128 grid cells in the radial direction, respectively. Fig. 14 shows the film thickness computed using these four different grids. The vertical lines in Fig. 14 indicate the locations where the spatial error is quantified, see the inset. For a grid with size of Δx, the relative error $e_{\Delta x}$ is defined as

$$e_{\Delta x} = \left| \frac{h_{\Delta x \to 0} - h_{\Delta x}}{h_{\Delta x \to 0}} \right|, \tag{20}$$

where $h_{\Delta x}$ is the computed film thickness and $h_{\Delta x \to 0}$ is the spatial error free film thickness predicted using Richardson's extrapolation. As can be seen in the inset of Fig. 14, the numerical method is formally first order in space in spite of the fact that central differences are used to approximate the spatial derivatives. This reduced order of accuracy is mainly attributed to the smoothing of the quantities at the interface. It is found that the grid with 64 grid cells in the radial direction is sufficient to resolve the film thickness within a relative error margin of 5% for the base case. Thus the computations are performed using this grid for all the results presented in the paper except for the low capillary number cases, i.e., $Ca < 0.004$. In the low Ca cases, a twice finer grid containing 128 grid cells in the radial direction is utilized in order to better resolve the thin liquid film region. Note that the finer grid with 128 grid cells in the radial direction reduces the error margin below 3% for the base case. It is emphasized here that 5% error is the largest error in the film thickness that is usually highly localized and the relative error is much smaller in the other parts.

A.2. Effects of density and viscosity ratios

Computations are then performed to show the effects of the density and viscosity ratios in the range $1 \leqslant \rho_o/\rho_b, \mu_o/\mu_b \leqslant 100$ for the clean and soluble cases. All other parameters are set to the values in the base case. As can be seen in Fig. 15, the relative change in the film thickness becomes negligible (below 0.6%) when the density and viscosity ratios $\rho_o/\rho_b \geqslant 10$, $\mu_o/\mu_b \geqslant 10$. Therefore computations are performed with $\rho_o/\rho_b = \mu_o/\mu_b = 10$ in order to relax the time step restriction in all the results presented in this paper.

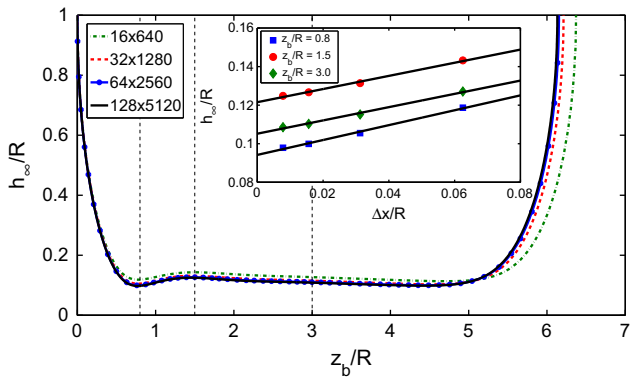

Fig. 14. Grid convergence. The film thickness computed for the base case using various computational grids ranging between 16×640 and 128×5120. The symbols in the inset show the film thickness computed at three locations indicated by dashed vertical lines for various grid cell sizes and the solid line is the linear least-squares fits to the numerical values.

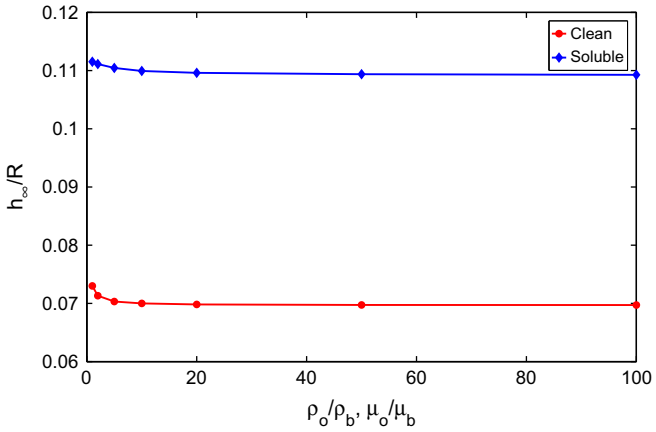

Fig. 15. Sensitivity of film thickness for the density and viscosity ratios in the range $1 \leqslant \rho_o/\rho_b, \mu_o/\mu_b \leqslant 100$ for the clean and soluble cases. All other parameters are set to the values in the base case.

References

Aussillous, P., Quere, D., 2000. Quick deposition of a fluid on the wall of a tube. Phys. Fluids 12, 2367–2371.

Beresnev, I., Gaul, W., Vigil, R., 2011. Thickness of residual wetting film in liquid–liquid displacement. Phys. Rev. E 84, 026327.

Bretherton, F.P., 1961. The motion of long bubbles in tubes. J. Fluid Mech. 10, 166–188.

Campana, D.M., Ubal, S., Giavedoni, M., Saita, F., 2010. Numerical prediction of the film thickening due to surfactants in the Landau–Levich problem. Phys. Fluids 22, 032103.

Chern, I.L., Glimm, J., Mcbryan, O., Plohr, B., Yaniv, S., 1986. Front tracking for gas dynamics. J. Comput. Phys. 62, 83–110.

Clift, R., Grace, J.R., Weber, M.E., 1978. In: Bubbles, Drops and Particles. Academic Press, New York.

Daripa, P., Pasa, G., 2009. The thickening effect of interfacial surfactant in the drag-out coating proble. J. Stat. Mech. – Thoery Exp., L07002.

Daripa, P., Pasa, G., 2010. The effect of surfactant on the motion of long bubbles in horizontal capillary tubes. J. Stat. Mech. – Thoery Exp., L02002.

Fairbrother, F., Stubbs, A.E., 1935. Studies in electroendosmosis: Part IV. The bubble-tube methods of measurements. J. Chem. Soc. 1, 527–529.

Fujioka, H., Grotberg, J.B., 2005. The steady propagation of a surfactant-laden liquid plug in a two-dimensional channel. Phys. Fluids 17, 082102.

Ghadiali, S.N., Gaver, D.P., 2003. The influence of non-equilibrium surfactant dynamics on the flow of a semi-infinite bubble in a rigid cylindrical capillary tube. J. Fluid Mech. 478, 165–196.

Giavedoni, M., Saita, F., 1997. The axisymmetric and plane cases of a gas phase steadily displacing a newtonian liquid – a simultaneous solution of the governing equations. Phys. Fluids 9, 2420–2428.

Ginley, G.M., Radke, C.J., 1989. Influence of soluble surfactants on the flow of long bubbles through a cylindrical capillary. ACS Symp. Ser. 396, 480–501.

Glimm, J., Graham, M.J., Grove, J., Li, X.L., Smith, T.M., Tan, D., Tangerman, F., Zhang, Q., 1998. Front tracking in two and three dimensions. Comput. Math. Appl. 35, 1–11.

Grotberg, J., 2001. Respiratory fluid mechanics and transport processes. Annu. Rev. Biomed. Eng. 3, 421–457.

Grotberg, J., 2011. Respiratory fluid mechanics. Phys. Fluids 23, 021301.

Halpern, D., Fujioka, H., Takayama, S., Grotberg, J.B., 2008. Liquid and surfactant delivery into pulmonary airways. Respir. Physiol. Neurobiol. 163, 222–231.

Harlow, F.H., Welch, J.E., 1965. Numerical calculation of time-dependent viscous incompressible flow of fluid with free surface. Phys. Fluids 8, 2182–2189.

Heil, M., 2001. Finite reynolds effects in the Bretherton problem. Phys. Fluids 13, 2517–2521.

Heil, M., Hazel, A., Smith, J.A., 2008. Mechanics of airway closure. Respir. Physiol. Neurobiol. 163, 214–221.

Hodges, S., Jensen, O., Rallison, J., 2004. The motion of a viscous drop through a cylindrical tube. J. Fluid Mech. 501, 279–301.

Johnson, R., Borhan, A., 2003. Pressure-driven motion of surfactant-laden drops through cylindrical capillaries: effect of surfactant solubility. J. Colloid Interf. Sci. 261, 529–541.

Krechetnikov, R., Homsy, G.M., 2005. Experimental study of substrate roughness and surfactant effects on the Landau–Levich law. Phys. Fluids 17, 102108.

Krechetnikov, R., Homsy, G.M., 2006. Surfactant effects in the Landau–Levich problem. J. Fluid Mech. 559, 429–450.
Levich, V.G., 1962. In: Physicochemical Hydrodynamics. Prentice Hall, Englewood Cliffs, NJ, USA.
Muradoglu, M., Tryggvason, G., 2008. A front-tracking method for computation of interfacial flows with soluble surfactants. J. Comput. Phys. 227, 2238–2262.
Otis, D.R., Ingenito, E., Kamm, R., Johnson, M., 1994. Dynamic surface tension of surfactant TA: experiments and theory. J. Appl. Physiol. 77, 2681–2688.
Park, C.W., 1992. Influence of soluble surfactants on the motion of a finite bubble in a capillary-tube. Phys. Fluids A – Fluid Dyn. 4, 2335–2347.
Peskin, C.S., 1977. Numerical analysis of blood flow in the heart. J. Comput. Phys. 25, 220–252.
Ramdane, O.O., Quere, D., 1997. Thickening factor in Marangoni coating. Langmuir 13, 2911–2916.
Ratulowski, J., Chang, H.C., 1989. Transport of gas bubbles in capillaries. Phys. Fluids A – Fluid Dyn. 1, 1642–1655.
Ratulowski, J., Chang, H.C., 1990. Marangoni effects of trace impurities on the motion of long gas-bubbles in capillaries. J. Fluid Mech. 210, 303–328.
Schurch, S., Bachofen, H., Goerke, J., Possmayer, F., 1989. A captive bubble method reproduces the in situ behavior of lung surfactant monolayers. J. Appl. Physiol. 67, 2389–2396.
Severino, M., Giavedoni, M.D., Saita, F.A., 2003. A gas phase displacing a liquid with soluble surfactants out of a small conduit: the plane case. Phys. Fluids 15, 2961–2972.
Severino, M., Campana, D., Giavedoni, M.D., 2005. Effects of a surfactant on the motion of a confined gas–liquid interface. The influence of the Peclet number. Latin Am. Appl. Res. 35, 225–232.
Shen, A., McKinley, B.G.G., Stone, H., 2002. Fiber coating with surfactant solutions. Phys. Fluids 14, 4055–4068.
Stebe, K.J., Barthes-Biesel, D., 1995. Marangoni effects of adsorption–desorption controlled surfactants on the leading end of an infinitely long bubble in a capillary. J. Fluid Mech. 286, 25–48.
Stone, H., 1990. A simple derivation of the time-dependent convective-diffusion equation for surfactant transport along a deforming interface. Phys. Fluids 2, 111–112.
Stone, H.A., 1994. Dynamics of drop deformation and breakup in viscous fluids. Ann. Rev. Fluid Mech. 26, 65–102.
Stone, H.A., Stroock, A., Ajdari, A., 2004. Engineering flows in small devices: microfluidics toward lab-on-a-chip. Ann. Rev. Fluid Mech. 36, 381–411.
Swaminathan, T., Mukundakrishnan, K., Ayyaswamy, P., Eckmann, D., 2010. Effect of a soluble surfactant on a finite-sized bubble motion in a blood vessel. J. Fluid Mech. 642, 509–539.
Tasoglu, S., Demirci, U., Muradoglu, M., 2008. The effect of soluble surfactant on the transient motion of a buoyancy-driven bubble. Phys. Fluids 20, 040805.
Taylor, G.I., 1961. Deposition of a viscous fluid on the wall of a tube. J. Fluid Mech. 10, 161–165.
Tryggvason, G., Bunner, B., Esmaeeli, A., Juric, D., Al-Rawahi, N., Tauber, W., Han, J., Nas, S., Jan, Y., 2001. A front-tracking method for the computations of multiphase flow. J. Comput. Phys. 169, 708–759.
Unverdi, S.O., Tryggvason, G., 1992. A front-tracking method for viscous, incompressible, multi-fluid flows. J. Comput. Phys. 100, 25–37.